

A 6-DOF isotropic measuring system for force and torque components of drag for use in wind tunnels

Innovative design

V. Portman · B. Z. Sandler ·
V. Chapsky · I. Zilberman

Received: 14 September 2009 / Accepted: 19 October 2009 / Published online: 28 November 2009
© Springer Science+Business Media, B.V. 2009

Abstract A 6-DOF isotropic device for measurement of force and torque components of drag that is suitable for use in wind tunnels is described in this paper. With our system, only the body under investigation and its fastening elements are placed inside the wind tunnel; six force sensors (load cells) are fastened outside the wind tunnel in a symmetric design by means of a metal cubic frame suspended on a massive base. Mathematical expressions describing the measurement and computation process of the values of the six force and torque vectors of the above-mentioned sensors are proposed. The isotropy features of the proposed device were shown to be superior to those of an existing tunnel balance device. To test the proposed device, the influence of the air flow on a model pattern in the shape of a flat disc or a cube fastened along its diagonal, the patterns were positioned at different angles relative to the air flow in the tunnel.

Keywords 6-DOF force/torque sensor · Wind tunnel · External balances · Isotropic sensor system

1 Brief overview of air flow studies

Means for determining the forces and torques acting on bodies traveling at high speeds or subjected to variable airflows in wind tunnels and for investigation of behavior of the airflow are required by both science and industry. The influence of the airflows on a body (or system of bodies) is used as a measure of the parameters of the air resistance acting on this body (or system of bodies). Drag forces and torques, lifting or carrying forces and torques, and the “air attacking angle” (the angle between the surface of the body and the air flow) are examples of such parameters.

Figure 1 shows the three tunnel balances that are usually applied for measuring wind drag. The typical features of these six-component tunnel balances include: (i) simultaneous and independent measurement of normal, axial and side forces and pitch, roll, and yaw moments; and (ii) calibration of all interaction terms with combined linearity, hysteresis, and repeatability accuracies of 0.1% of the full scale.

Normally, the airflow forces acting on a wind tunnel model are described relative to a Cartesian coordinate system, which is fixed either to the model or the free stream directions. In the case of an “internal balance”, the forces transmitted by the

V. Portman · B. Z. Sandler (✉) · V. Chapsky ·
I. Zilberman
Ben-Gurion University of the Negev, Beer-Sheva, Israel
e-mail: sandler@bgu.ac.il

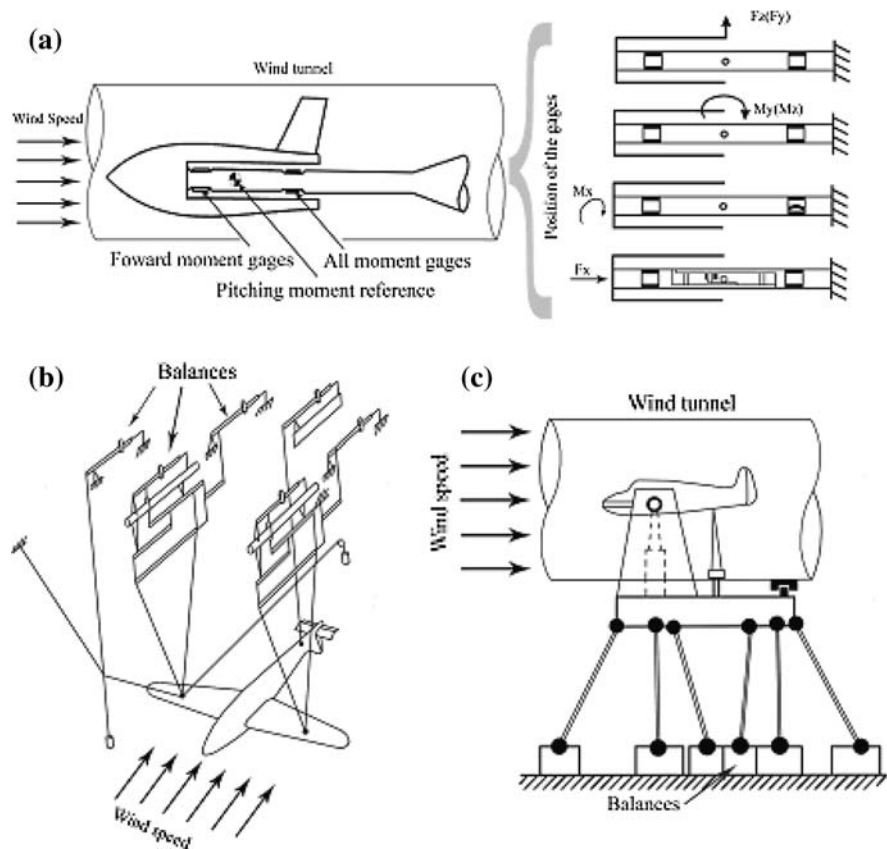
V. Portman
e-mail: portman@bgu.ac.il

V. Chapsky
e-mail: chapsky@bgu.ac.il

I. Zilberman
e-mail: zilyag@gmail.com

Fig. 1 Layouts of the three main force and torque measuring devices used in wind tunnels. Partly adapted from Ewald (2000) and Corliss and Cole (1998).

a The model is attached, via a spring, to a mounting sting carrying strain gauges. **b** The model is suspended from lever-type devices located in the tunnel. **c** The model is placed on a platform inside the tunnel, and the forces are measured with 6-DOF hexapod-like balances placed outside the tunnel



mounting sting are measured by strain gauges. This set-up, which is the one of the most widespread measuring methods used in wind tunnels for six or fewer load components, is shown in Fig. 1a. The set-up has three inherent problems. The first is the interaction between the strain gauge resistances measured for different loads. To address this problem (at least partially), a special rectangular design of the strain-gauge balance has been suggested, in which the positioning of the strain gauges provides the required partial separation between forces and bending moments, thereby facilitating a reduction in interference.

The second problem is the anisotropy appearing in the measurements. This anisotropy is due to the fact that the stretching-pressing stresses depend upon the cross-section area of the beam, whereas the bending stresses depend upon the moments of inertia I_y and I_z of the cross-sections. As a result, the values of axial and cross forces differ by orders of magnitude. By analogy, the torsion and bending moments around the coordinate axes differ markedly.

The third problem is that the signal from each strain gauge bridge is proportional not only to the component to which this bridge is assigned, but also (linearly or non-linearly) to a small but complicated mixture of signals of all the other components. This latter problem requires sophisticated calibration methods and a mathematical description of the behavior of the bridge (Ewald 2000). Many of the coefficient evaluation methods in use today are influenced by earlier thinking when computers were not available (Ewald 2000). In these methods, the loads are applied in a loading sequence for one pure component, while all the other components are zero or at least constant. The matrix coefficients are then evaluated by least-square error methods and compiled step by step.

In the custom model and sting attachment design of an internal balance (Ewald 2000) that we will use as our reference design for purposes of comparison, the tail of the model is connected, via a metallic spring, to the mounting sting (Fig. 1a). This mounting sting serves as a beam, whose bending and torsion is measured.

Corliss and Cole (1998) extended the second-order equations used in the model described above to a third-order mathematical description. Another type of internal six-component wind-tunnel balance is that having three-dimensional mechanisms, as described by Gorlin and Slezinger (2000). In this case, different points of the model under investigation are suspended on the levers of the balance mechanisms (a set-up that disturbs the air flow in the tunnel to some extent) that measure forces and torques caused by the wind in the tunnel, as shown in Fig. 1b. However, this configuration also gives rise to interference effects. To address this problem, some automatic calibration rigs for internal strain gauge balances have been developed (Pope and Harper 1999). The idea underlying these devices is shown in Fig. 1b. In this type of set-up, the calibrated balances are loaded by pneumatic cylinders located on a frame suspended on six load cells.

One of the many important fields requiring accurate information on airflow is civil engineering, since many structures have the potential to create “unpleasant” or even dangerous responses, depending on factors such as wind speed and direction and changes in the oscillation frequency of the structure. To design cladding systems for high-rise and medium-rise buildings, reliable prediction of the external wind pressures acting on the building surface is obtained by conducting by wind tunnel tests. Such tests can determine, for instance, the instantaneous point of air pressure application and aerodynamically significant torsion effects and can also predict the building overturning moments and small movements or displacements of the building. To meet these needs, a family of airflow study devices has been developed for civil engineering needs (Bentur et al. 1997).

Another scenario in which measurement facilities are sometimes needed is that of aerodynamic forces applied to bodies in the form of short-duration impulses. An example of the type of device required for this purpose is the six-component stress wave force balance used for measuring the forces on a model of the Japanese HYFLEX (HYpersonic FLight EXperiment) vehicle in a wind tunnel (Sanderson and Simmons 2006).

Yet another application may be found in the study of Tuttle et al. (1994) for the design of balance layouts. They made use of a wind tunnel for measurements of forces and torques on layouts

comprising closed-kinematic chains (or parallel kinematics). The latter are generally sturdier and more precise than open-chain robots. These kinds of layout balances are used in aerodynamic tunnels (Nguyen et al. 1992; Kerr 1989). Here, the external loadings are applied to a Stewart platform located outside the tunnel, and the output is monitored by the appropriate transducers. An example of this kind of device is shown in Fig. 1c. This approach can also be found in Allied Aerospace force measurement systems¹

Measurements that can be recorded in the air tunnel include the air (or liquid) and surface friction drag, acceleration, and lifting and lowering forces. From the examples described in this overview, it is clear that the measurement devices are designed such that they are connected to the pattern under investigation in the wind tunnel. An additional problem is that the algorithms translating the signals of the sensors have to be tailored to each specific case.

The main purpose of this paper is to describe a device comprising a measuring element combined with a computer for determining drag forces on a body in a wind tunnel. The device consists of a rectangular frame suspended on six load cells, which are located outside tunnel. The device uses the corresponding functions (or equations) for each of six force and moment components, depending upon the air speed and the shape of the body. Some ideas of this kind were discussed in Chapsky et al. (2007) and Liu and Tso (2002).

The proposed device for measuring forces and torques caused by airflow acting on a model located in a wind tunnel is characterized by following features:

- only one rod is placed in the tunnel for fastening the model, thus creating minimal disturbances to the flow;
- the balance and the measuring sensors are located outside the tunnel and supply information to computer, which is controlled by a program written particularly for this system;

¹ “Balances: Force & Moment, Internal and External Full Calibration Systems and Services”, Allied Aerospace, 7340 Trade St., Suite D, San Diego, CA 858-537-2020x301, www.fms-sd.com.

- the values of the forces and torques acting at the measuring point are automatically shown on the computer's screen for different air speeds;
- there are no interactions between the six measured values (as is often the case in existing tunnels).

2 Experimental set-up

2.1 System layout

A general view of the wind tunnel laboratory built at the Department of Mechanical Engineering of Ben-Gurion University of the Negev, Israel is shown in Fig. 2.

The maximal air speed in this tunnel is 40 m/sec. The length of the tunnel is about 30 m, and its cross-section is $0.7 \times 0.7 \text{ m}^2$. An aluminum frame, mounted around the tunnel, supports a single rod to which the pattern is fastened inside the tunnel. The frame is suspended at three of its four vertexes by means of six (one pair for each of three force directions) S-beam load cells of electronic 34970 data-loggers (Fig. 3), i.e., the force measuring devices are located outside the wind tunnel.

The pattern to be investigated is fixed at the mid-point of the vertical rod. Figure 4a shows one possible configuration for the locations of the pattern and the movable frame. The other possible configuration—that is used in the present study—is the symmetrical design shown in Fig. 4b.

The distinguishing characteristic of the proposed device (case b) is the symmetry of the balance device (as it is usually called), which is provided by:

1. Symmetrical distribution of the proof mass.
2. Orthogonal and symmetrical location/orientation of the directions of the measuring sensors.
3. Orthogonal and symmetrical location/orientation of the directions/attachments of the reactions of support system.

This symmetry facilitates the equivalence of the dynamic properties in all directions of the design and simplifies the processing the obtained results.

The wind creates a system of drag forces acting on the pattern. Three linear forces P_x , P_y and P_z along the corresponding coordinate axes, and three torques M_x , M_y and M_z around the same axes are measured. The measurement results are described as a 6×1 force–moment vector, expressed in the coordinate system associated with the basic frame, whose origin lies at the pattern fastening point.

$$\mathbf{P} = (P_x, P_y, P_z, M_x, M_y, M_z)^T \quad (1)$$

where P_x , P_y and P_z are force components along the X-, Y-, and Z-axes, and M_x , M_y , and M_z are torque components around the same axes. The six reaction forces $N_1, N_2 \dots N_6$, of the load cells acting on the aluminum frame are measured. In the general case, the balance of forces and moments that act on the aluminum frame to which the pattern is fastened may be expressed by the following matrix equation:

Fig. 2 General view of the wind tunnel



Fig. 3 Data-Logger of the 34970 type. **a** S-beam load cell. **b** View of a suspension including the Data-Logger

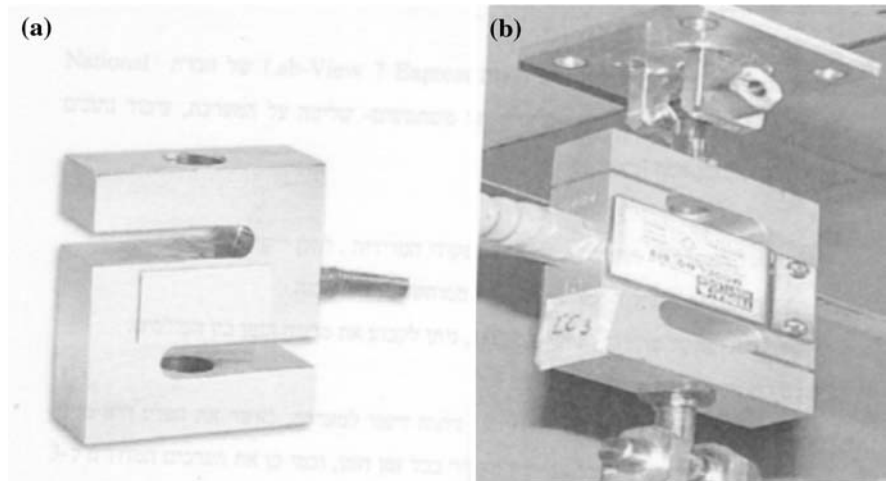
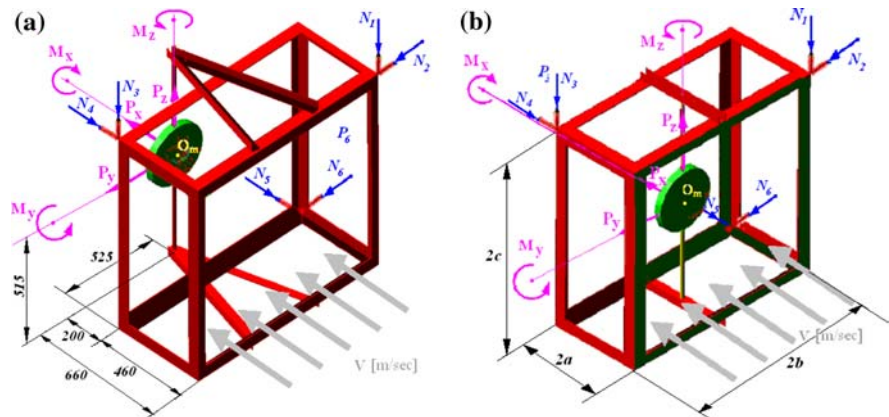


Fig. 4 Lay-out of the movable frame mounted around the tunnel. **a** Experimental case. **b** Ideal, space-symmetrical case



$$\begin{pmatrix} P_x \\ P_y \\ P_z \\ M_x \\ M_y \\ M_z \end{pmatrix} = \begin{pmatrix} \lambda_{x1} & \lambda_{x2} & \cdots & \lambda_{x6} \\ \lambda_{y1} & \lambda_{y2} & \cdots & \lambda_{y6} \\ \lambda_{z1} & \lambda_{z2} & \cdots & \lambda_{z6} \\ m_{x1} & m_{x2} & \cdots & m_{x6} \\ m_{y1} & m_{y2} & \cdots & m_{y6} \\ m_{z1} & m_{z2} & \cdots & m_{z6} \end{pmatrix} \begin{pmatrix} N_1 \\ N_2 \\ N_3 \\ N_4 \\ N_5 \\ N_6 \end{pmatrix} \quad (2)$$

where λ_{xi} , λ_{yi} , and λ_{zi} are directional cosines of the vectors N_i , ($i = 1, \dots, 6$), and m_{xi} , m_{yi} , and m_{zi} are moments of the unit vectors of the directions of the forces of reaction relative to the X-, Y-, and Z-axes.

Thus, the components of the forces and moments acting the pattern can be calculated simply from the measurements acquired by the six load cells.

A DAQ module was used for data acquisition. Data processing was performed by means of the LabView program. A view of the computer screen during the functioning of the wind tunnel at the beginning of the data gathering process is shown in Fig. 5. The layout

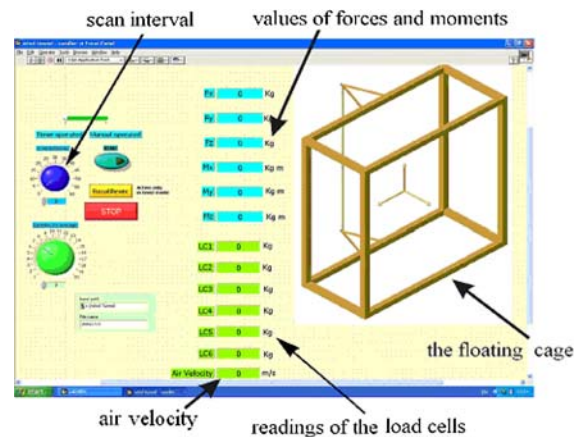


Fig. 5 The computer screen for data acquisition and processing during experiments in the wind tunnel

of the computer screen was designed such that the readings of the load cells and the calculated components of the forces and moments acting on the pattern

can be viewed simultaneously. The required parameters of the digital signal processing can be chosen by means of the screen tools.

The proposed system has following main advantages over the traditional string-based structure of strain gauges: simplicity in terms of structure and use, high reliability [due to the homogeneity of the measuring devices (six identical load cells) and shielding from temperature disturbances].

2.2 Evaluation of system anisotropy

The anisotropy of a structure can be estimated as the ratio of maximal to minimal stiffness values. In this work, the stiffness values described by six elements of the principal diagonal of the stiffness matrix were used for comparison of the stiffness properties of the devices. The diagonal elements describe the so-called collinear stiffness values (CSV) when force–moment reactions and a unit displacement of the body are measured along the same coordinate axes. Calculation of the CSV is based on the 6×6 external stiffness matrix K_{ex} of the devices. The external stiffness matrix of the proposed device (Fig. 4b) is:

$$K_{ex} = 2k \times \begin{pmatrix} 1 & 0 & 0 & 0 & 0 & 0 \\ 0 & 1 & 0 & 0 & 0 & 0 \\ 0 & 0 & 1 & 0 & 0 & 0 \\ 0 & 0 & 0 & (b^2 + c^2) & -ab & ac \\ 0 & 0 & 0 & -ab & (a^2 + c^2) & -bc \\ 0 & 0 & 0 & ac & -bc & (b^2 + a^2) \end{pmatrix} \quad (3)$$

where k is the stiffness value of a support (for the case in which all load cells are identical), and a , b , and c are the distances between the supports (between the axes of the load cells) located along the X -, Y -, and Z -axes, respectively (Fig. 4b). The external stiffness matrix of the device shown in the Fig. 1a is:

$$K_{ex} = \begin{pmatrix} \frac{a^2 E}{L} & 0 & 0 & 0 & 0 & 0 \\ 0 & \frac{a^4 E}{L^3} & 0 & 0 & 0 & \frac{a^4 E}{2L^2} \\ 0 & 0 & \frac{a^4 E}{L^3} & 0 & -\frac{a^4 E}{2L^2} & 0 \\ 0 & 0 & 0 & \frac{a^4 G}{6L} & 0 & 0 \\ 0 & 0 & -\frac{a^4 E}{2L^2} & 0 & \frac{a^4 E}{3L} & 0 \\ 0 & \frac{a^4 E}{2L^2} & 0 & 0 & 0 & \frac{a^4 E}{3L} \end{pmatrix} \quad (4)$$

where L is the length of the beam, a is the side length of the square cross-section of the beam, E is Young's modulus, and G is the modulus of rigidity.

The stiffness anisotropy of the devices is evaluated in terms of an anisotropy index η , which is equal to the ratio of the maximal and minimal stiffness values. In this paper, two types of indexes are considered separately:

- The index of translational stiffness values (TSV)

$$\eta_{tr} = \frac{\max(k_{ii})}{\min(k_{ii})}, \quad i = 1, 2, 3 \quad (5)$$

- The index η_{rot} of rotational stiffness values (RSV)

$$\eta_{rot} = \frac{\max(k_{ii})}{\min(k_{ii})}, \quad i = 4, 5, 6 \quad (6)$$

where k_{ii} ($i = 1, \dots, 6$) is an element in the i th row (column) of the principal diagonal of matrices K_{ex} (Eqs. 3 and 4).

Matrices (3) and (4) yield the following values of the anisotropy indexes for the two devices being compared:

$\eta_{tr} = \begin{cases} \frac{k_{11}}{k_{22}} = 1, \\ \frac{k_{11}}{k_{22}} = \frac{L^2}{a^2}, \end{cases}$	for the device in Fig. 4b for the device in Fig. 1a
$\eta_{rot} = \begin{cases} \frac{k_{44}}{k_{55}} = \frac{b^2 + c^2}{a^2 + c^2}, \\ \frac{k_{66}}{k_{44}} = \frac{2E}{G} \approx 5, \end{cases}$	for the device in Fig. 4b for the device in Fig. 1a

The numerical results of the stiffness comparison are shown in Table 1.

It is clear from Table 1 that the isotropy features of proposed arrangement—the device shown in

Table 1 Isotropy indexes for the devices shown in Figs. 1a and 4b

Parameter	Symbol	Device in Fig. 4b	Device in Fig. 1a
TSV anisotropy	η_{tr}	1	~ 50 – 100
RSV anisotropy	η_{rot}	1^a – 1.7^b	~ 5

^a For the ideal case: $a = b = c$

^b For a real case: $a = 230$ mm, $b = 525$ mm, $c = 515$ mm

Fig. 4b—are superior, i.e., characterized by smaller values of the anisotropy indexes. Furthermore, the proposed arrangement of the device gives the possibility to reach full isotropy in stiffness properties, as shown in Fig. 6.

3 Description of the experiments

In experiments executed in the wind tunnel with a real arrangement of the frame (Fig. 4a), the following two patterns were tested:

- A disk of diameter 320 mm located:
- perpendicular to the flow direction;
- inclined at about 45° to the flow direction; or
- parallel to the flow direction.
- A Perspex cube with a rib of 200 mm fastened diagonally on the vertical measuring rod.

Figure 7 shows the location of the patterns in the wind tunnel.

The following equation was used for calculation of the components of the generalized force for the real arrangement (Fig. 4a), according Eq. 2:

$$\begin{pmatrix} P_x \\ P_y \\ P_z \\ M_x \\ M_y \\ M_z \end{pmatrix} = \begin{pmatrix} 0 & 0 & 0 & -1 & -1 & 0 \\ 0 & 1 & 0 & 0 & 0 & 1 \\ -1 & 0 & -1 & 0 & 0 & 0 \\ 525 & -515 & -525 & 0 & 0 & 515 \\ -660 & 0 & -200 & -515 & 515 & 0 \\ 0 & -660 & 0 & 525 & -525 & -200 \end{pmatrix} \begin{pmatrix} N_1 \\ N_2 \\ N_3 \\ N_4 \\ N_5 \\ N_6 \end{pmatrix} \quad (7)$$

Graphs of the forces and moments for different wind speeds in the tunnel are presented in Figs. 8, 9, 10, 11, 12, 13, 14, 15. Figures 8 and 9 show the change of forces and moments as a function of the wind speed for the case in which the disk is located perpendicular to the flow direction. In this case, the force P_x changes according to the second power of the wind speed (graph “Poly”: $(P_x) \rightarrow y = 0.007x^2 - 0.0009x - 0.0258$) and coincides well with Bernoulli’s Law (black line on the upper curve in Fig. 8). The regression coefficient, which shows the degree of coincidence between real and approximated curves, is 0.9997. The forces P_y and P_z are relatively small and may be attributed to turbulence.

The theoretical curve is calculated from Bernoulli’s Law:

$$(P_x)_{\text{theor}} = \rho \frac{v^2}{2} A_L \quad (8)$$

where $(P_x)_{\text{theor}}$ is the drag force attributed to the airflow acting on the disk or cube in the direction parallel to the longitudinal axis of the tunnel (air flow), ρ is the density of air ($\rho = 1.293 \text{ kg/m}^3$ at 0°C and atmospheric pressure), v is the wind speed in the tunnel (taken from the graphs), and A_L is the area of the pattern’s projection on the plane perpendicular to the longitudinal axis of the tunnel. When the disk is located perpendicular to the flow direction, $A_L = \pi r^2$, where r , the effective radius of the disk, $\approx 0.16 \text{ m}$.

Figure 9 shows the moments around the axes. M_x is small and may be attributed to turbulence, while moments M_y and M_z are almost equal and follow Bernoulli’s Law.

Figures 10 and 11 show the change of forces and moments as a function of the wind speed for the case in which the disk is positioned at 45° to the flow direction.

As is clear from Fig. 10, the drag forces P_x and P_y are close to Bernoulli’s Law, the values being approximately half those of the previous case; the regression coefficients (black lines in Fig. 10) are about 0.9989 and 0.9993, respectively. The third force P_z is close to zero.

Figures 12 and 13 show the change of forces and moments as a function of the wind speed for the case in which the disk positioned at 90° to the flow direction.

We also measured the airflow resistance caused by a cubic body located in the wind tunnel. The forces and moments for this experiment are shown in Figs. 14 and 15, respectively. The behavior of the drag force component P_x corresponds to its

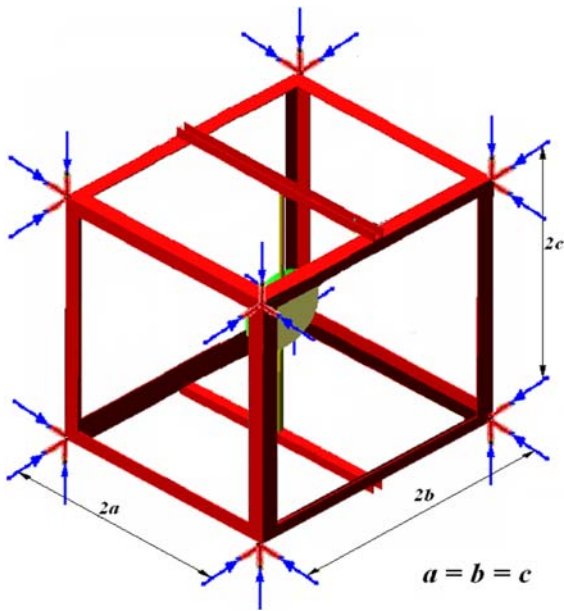


Fig. 6 Fully isotropic design of the frame with equal sides and 24 symmetrically located supports

Fig. 7 Location of the pattern in the wind tunnel. **a** Disk. **b** Cubic body (here, made of Perspex)

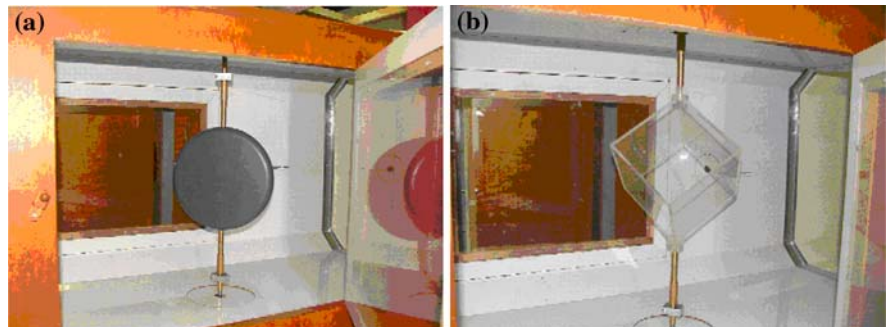
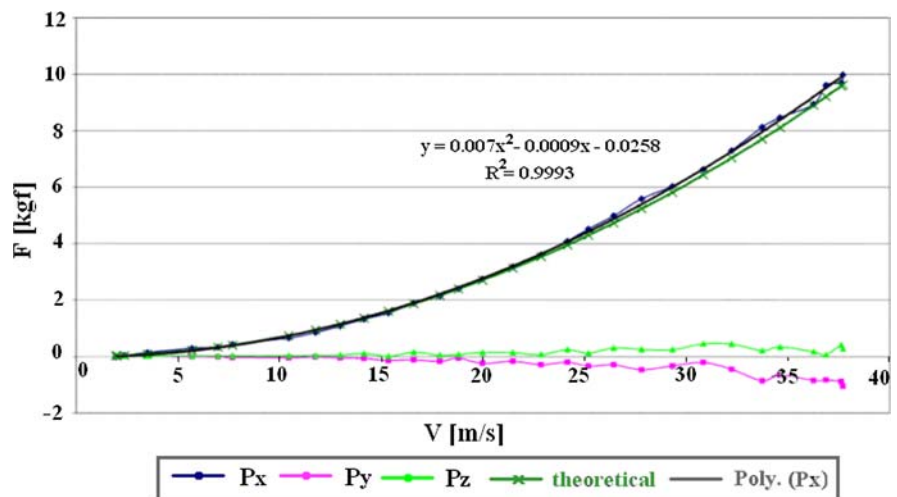


Fig. 8 Drag forces P_x , P_y , and P_z acting on the disk as function of the wind speed when the disk is located perpendicular to the flow direction. The dark green line is a parabolic approximation computed with minimal mean square error (Color figure online)



theoretical value, which is a parabolic approximation, according to Bernoulli's Law with regression coefficient 0.9969. P_y and P_z are almost zero.

Figure 15 shows the values of the moments M_y and M_z , which follow Bernoulli's Law and are close one to another, while M_x is practically zero.

Let us now consider a numerical example. Under the following conditions—a disk positioned at 45° to the air flow direction, wind speed v along the tube of 30 (m/s), density of the air $\rho = 1.293$ (kg/m³), disk projection area on the plane perpendicular to the air tube axis $\pi r^2 \cdot \cos 45^\circ$, and radius of the disk $r = 0.16$ (m)—the drag force in the X-direction according to Eq. 8 is:

$$\begin{aligned} P_x &= 0.5 \times [1.293(\text{kg/m}^3) \times (30(\text{m/s}))^2 \times \pi \\ &\quad \times 0.16^2(\text{m}^2)] \times \cos 45^\circ \\ &= 33(\text{N}) = 3.4(\text{kgf}) \end{aligned}$$

This experimental result is in good agreement with the calculated value (Fig. 10).

Fig. 9 Drag moments M_x , M_y , and M_z acting on the disk as function of wind speed when the disk located perpendicular to the flow direction

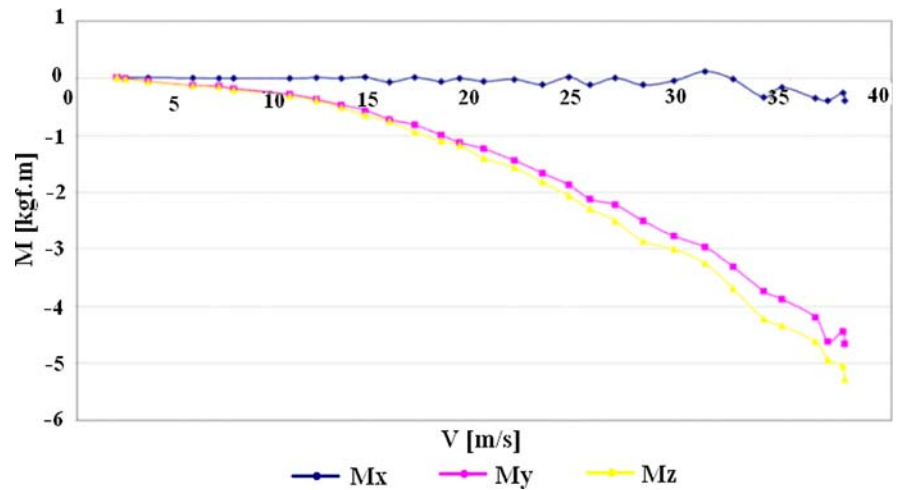


Fig. 10 Drag forces P_x , P_y , and P_z acting on the disk positioned at 45° to the airflow

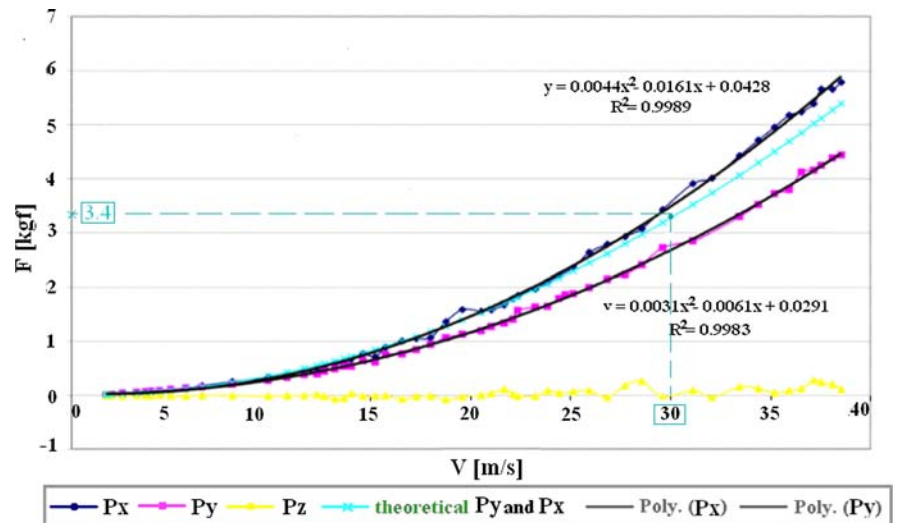


Fig. 11 Drag moments M_x , M_y , and M_z acting on the disk positioned at 45° to the airflow

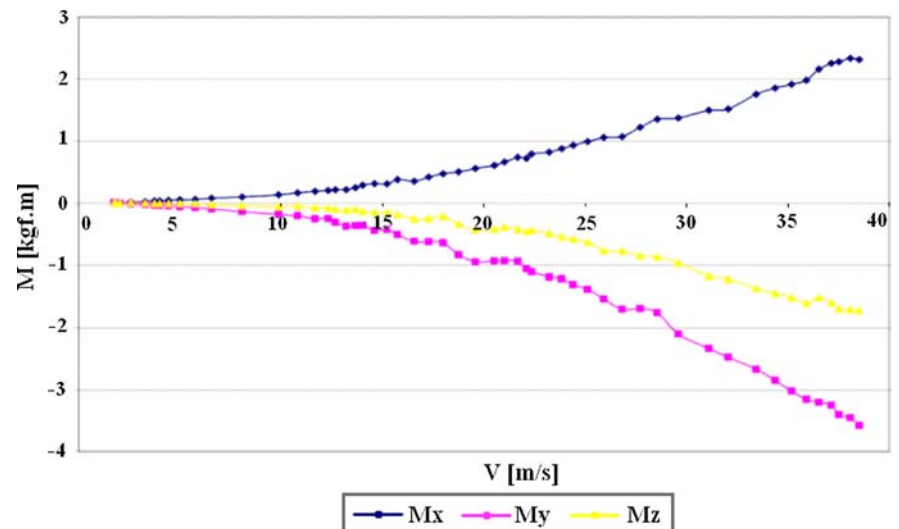


Fig. 12 Drag forces P_x , P_y , and P_z acting on the disc positioned along to the airflow

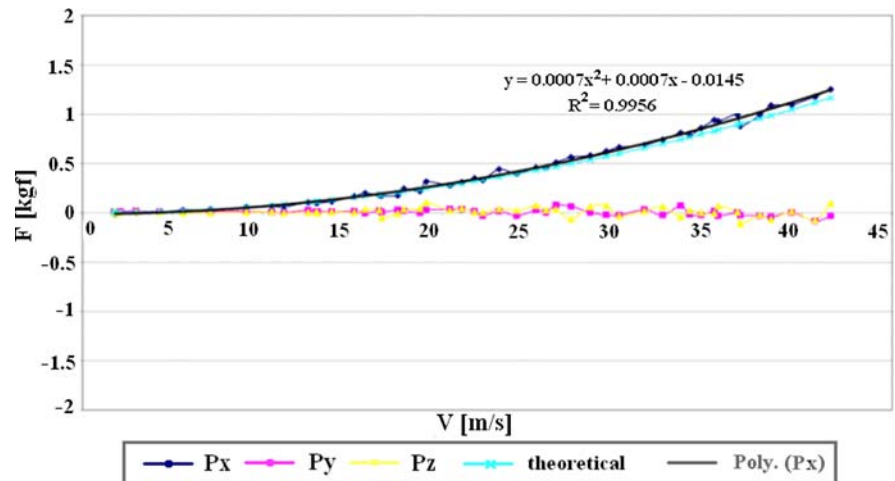


Fig. 13 Drag moments M_x , M_y , and M_z acting on the disk positioned along to the airflow

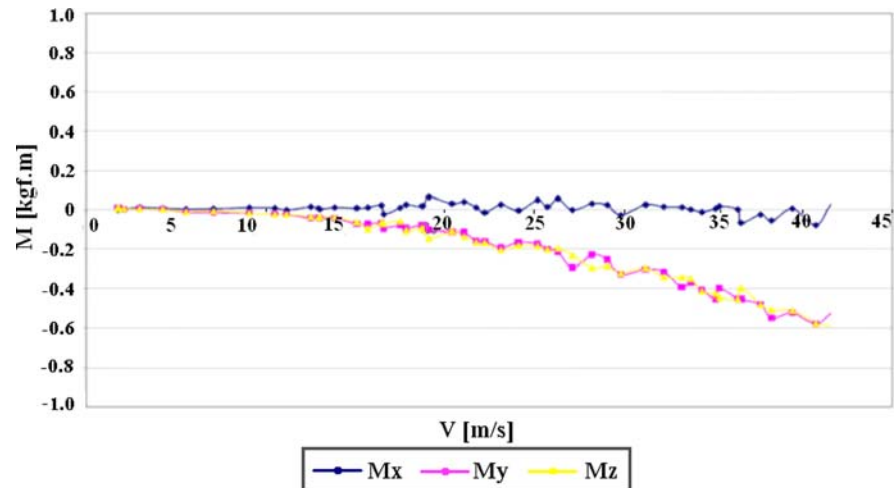


Fig. 14 Drag forces P_x , P_y , and P_z acting on the cubic body

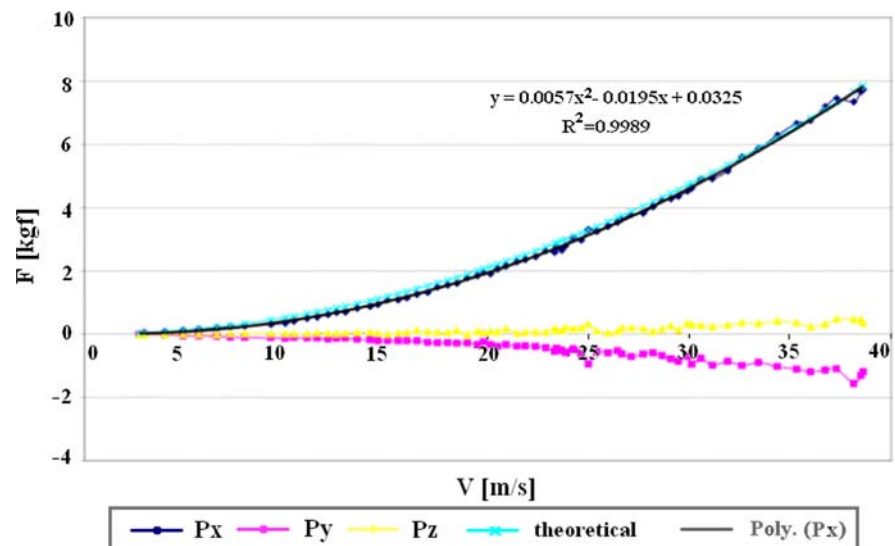
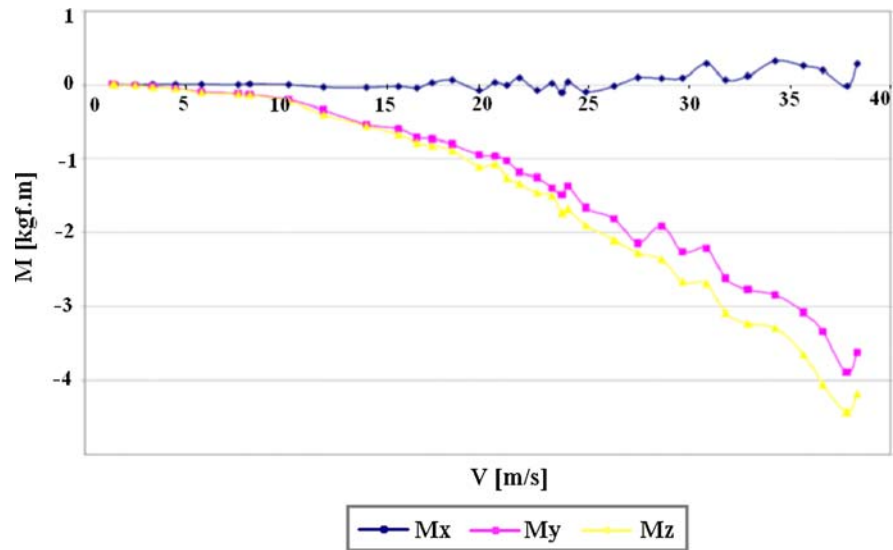


Fig. 15 Drag moments M_x , M_y , and M_z acting on the cubic body



4 Dynamic investigation of the proposed air drag measuring device

The purpose of the dynamic investigation of the proposed device was to define the frequency bandwidth for all the measured force–torque components acting on the pattern and to estimate the influence of the mass of the pattern on the measuring device. We chose to conduct a computerized dynamic simulation of a virtual model of the device, because of the cost efficiency of this method and because we did not have a real device meeting our particular conditions.

In the simulation, the virtual frame has the dimensions shown in Fig. 4b; the material of the frame is aluminum; and the mass of the frame m equals 16.0 kg. We consider identical load cells with the same stiffness and viscosity that were previously defined in the experiments with the real devices.

For definition of the stiffness, the real load cell was loaded with different loads, and its deformations were measured with a micrometer. The results of measurements are shown in Fig. 16. As is clear from this graph, the stiffness of the load cell is $k = 5000$ (N/mm).

The damping coefficient d of the load cell was calculated from the response of the real device (Fig. 4a) for an outer shock in the X -direction. The results of the measurement of the shock response are shown in the Table 2 and Fig. 17.

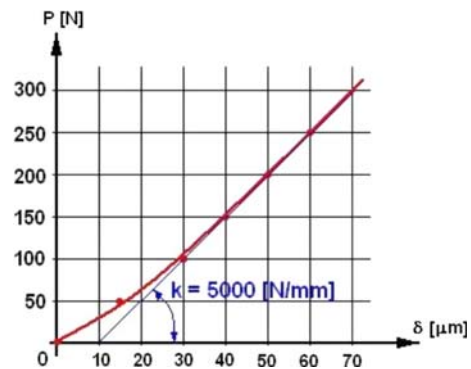


Fig. 16 Load cell deformation δ (μm) as function of the applied loading P (N)

Table 2 Measurements of the shock response

t_n (ms)	$x(t_n)$ (mU)	Δt (ms)	$x(t_n)/x(t_{n+1})$	γ	β (1/s)	d (N/(m/s))
75	520	—	—	—	—	—
200	50	125	10.4	2.34	18.72	150

t_n —time of measurements of signal values, $x(t_n)$ —measured value of the signal, Δt —time interval between two successive measurements, γ —logarithm of the ratio of two successive measured signal values, β —index of attenuation, where $\beta = \frac{\gamma}{\Delta t}$, d —damping coefficient of one load cell, where $d = m\beta/2$ (in the experiment two load cells $N4$ and $N5$ act in parallel in the X -direction)

The virtual model of the investigated apparatus was constructed by means of the interactive computer-based system ADAMS/View. The load cells



Fig. 17 Measurement of the shock response

were represented as spring-damper elements with stiffness and damping coefficients equal to previously measured values: $k = 5000$ (N/mm), and $d = 0.15$ (N/(mm/s)).

To investigate the dynamics of the device, harmonic forces and torques were applied to the center of mass of the pattern, which allocated in the frame center. Only one DOF was tested in each simulation. To plot the Bode graphs in the relevant frequency range, we need the Input function for the force or moment, which has a wide spectrum of frequencies. We chose a harmonic function with a linearly growing frequency as the Input function. The Output signals were measured as deformation forces and torques of the appropriate springs. The torques were measured relative to the corresponding axes. The following simulation parameters were chosen: the duration of simulation (parameter “End time”) = 0.5 s and the number of samples during simulation (parameter “Steps”) = 4000. Figure 18 presents the time-domain plots of the input force and a representative sample of the output response.

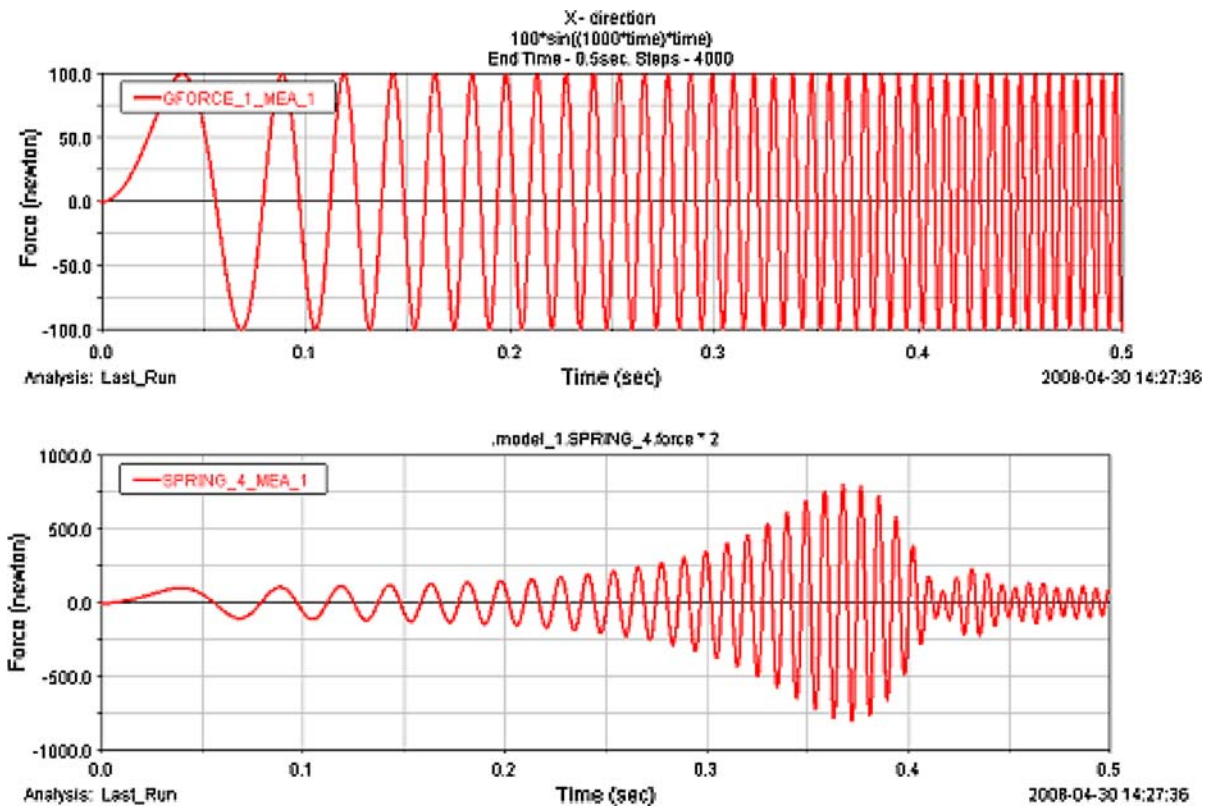


Fig. 18 Input force and its response in the X-direction in a time-domain representation

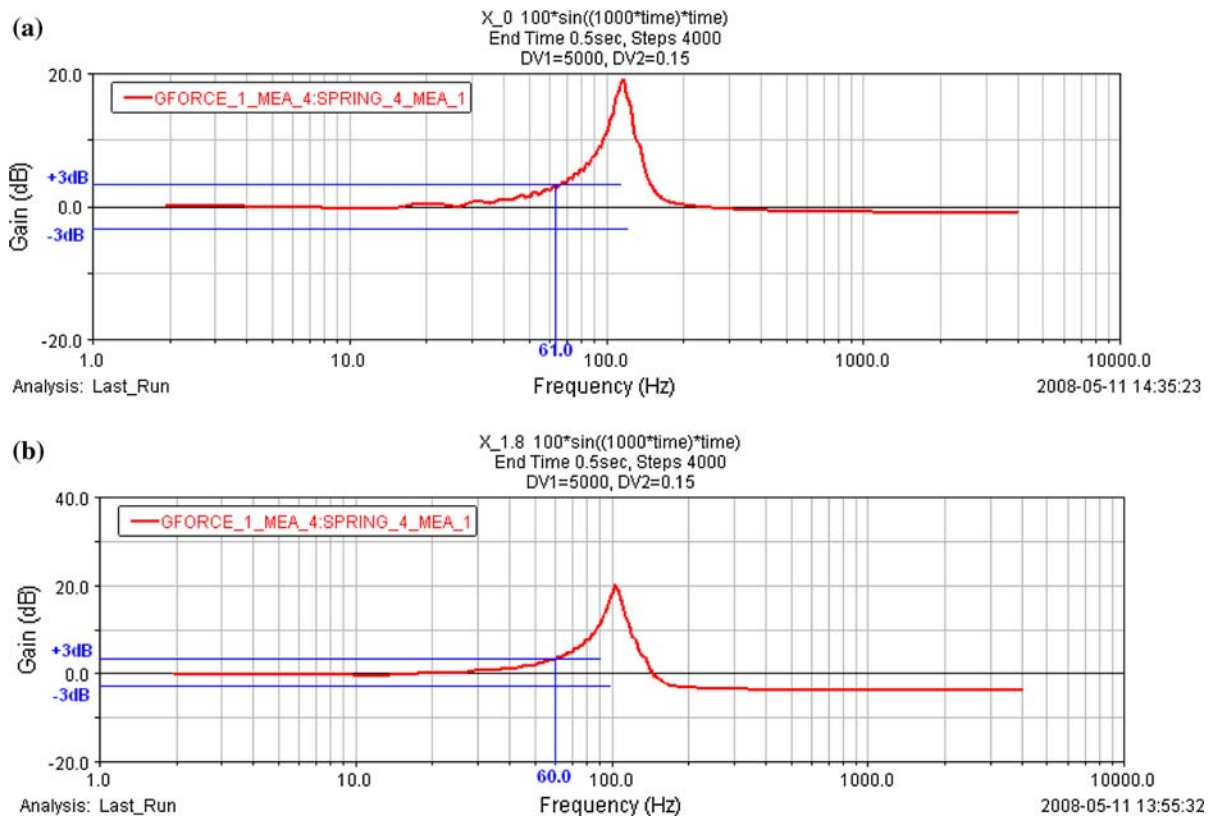


Fig. 19 Bode plots for investigation of the dynamics of the device in the X-, Y-, and Z-directions

Figure 19 shows the Bode plots for investigation of the response of the device in the X-, Y-, and Z-directions for a zero-mass pattern (investigation solely of the dynamics of Frame) (a) and for an aluminum pattern with a density of 2.7×10^3 (kg/m³) (b). The bandwidth was defined for all investigated oscillations as the frequency range in which the amplitude frequency-domain representation (Bode plot) did not exceed ± 3 dB.

As can be seen from the figures, the bandwidths for the real and simulated cases are close to one another (≈ 60 Hz), which means that the mass of the pattern does not influence the device's bandwidth.

Figure 20 shows the Bode plots for investigation of the response of the device around the X-, Y-, and Z-directions for zero-mass (a, c, e) and for aluminum (b, d, f) patterns.

We can conclude from these simulations that the bandwidth of the proposed device is 54 Hz (the minimal value obtained in the investigated cases) and

does not depend on the mass of commonly used patterns in the tunnel.

5 Conclusions

1. The proposed device uses the same standard sequence, irrespective of the type of pattern, and requires only a simple action for obtaining the measured data. The investigator must simply fasten the pattern on the rod.
2. Dynamic estimations of the virtual model of the proposed tunnel balance by means of the interactive computer-based ADAMS/View system showed that the working frequency of the proposed method and device are limited to a bandwidth of 50–60 Hz.
3. The translational isotropy of the proposed device is defined by the independence of the sensitivity

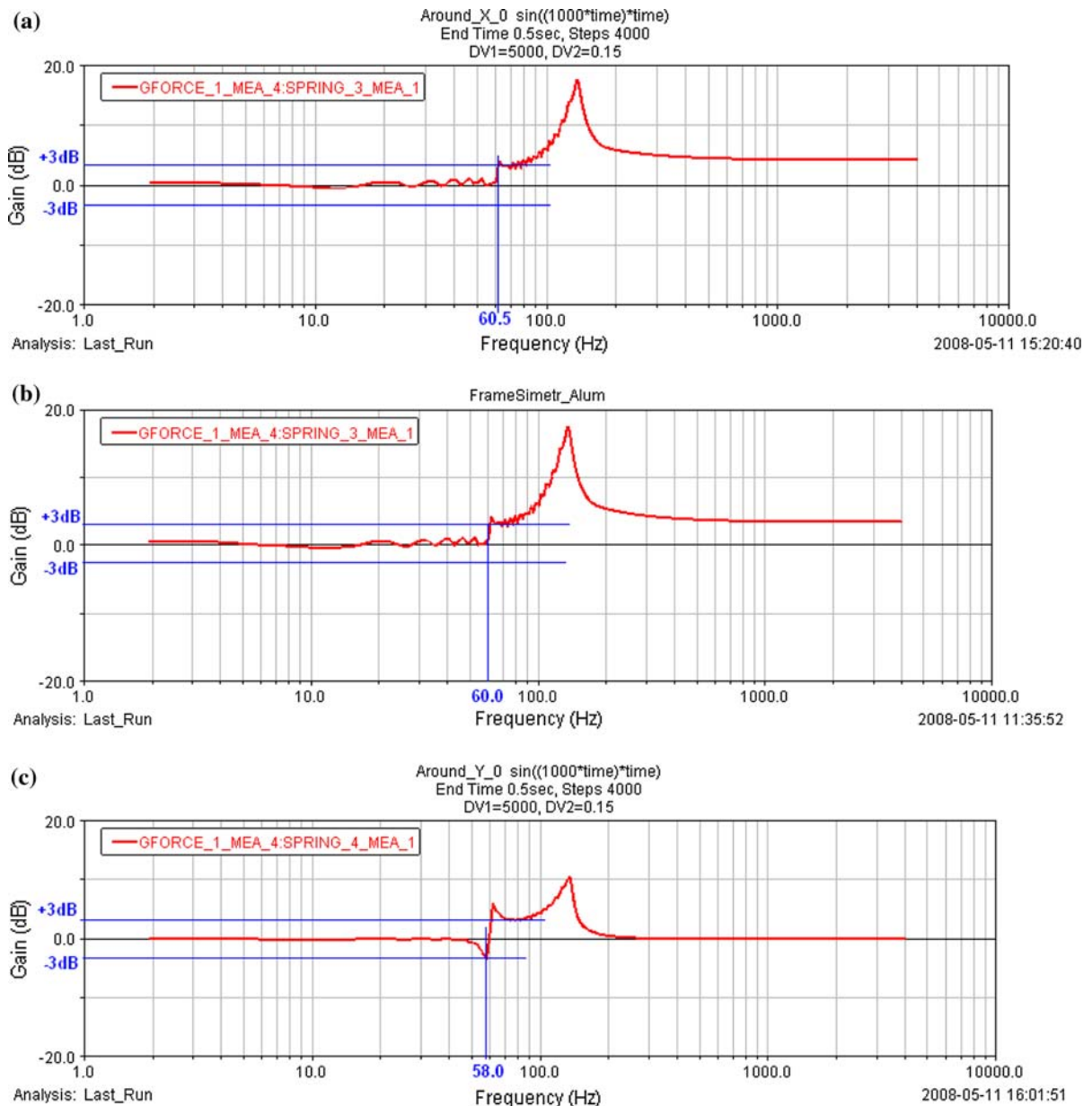


Fig. 20 Bode plots for investigation of the device's response around the X-, Y-, and Z-directions

of measurement on the direction of the operating forces.

4. For estimation of the anisotropy of the devices, the anisotropy index, i.e., the ratio of maximum to minimum stiffness values, is applied. Two types of index were used—translational and rotational stiffness values (see Table 1).
5. The proposed device has better isotropic features than conventionally used systems: it is

fully isotropic from the point of view of translational stiffness and has a high level of isotropy from the view point of rotational stiffness.

6. The proposed approach facilitates the design of a completely isotropic measuring system with 24 identical symmetrically located supports. However, it is necessary to balance the extra costs against the increased precision.

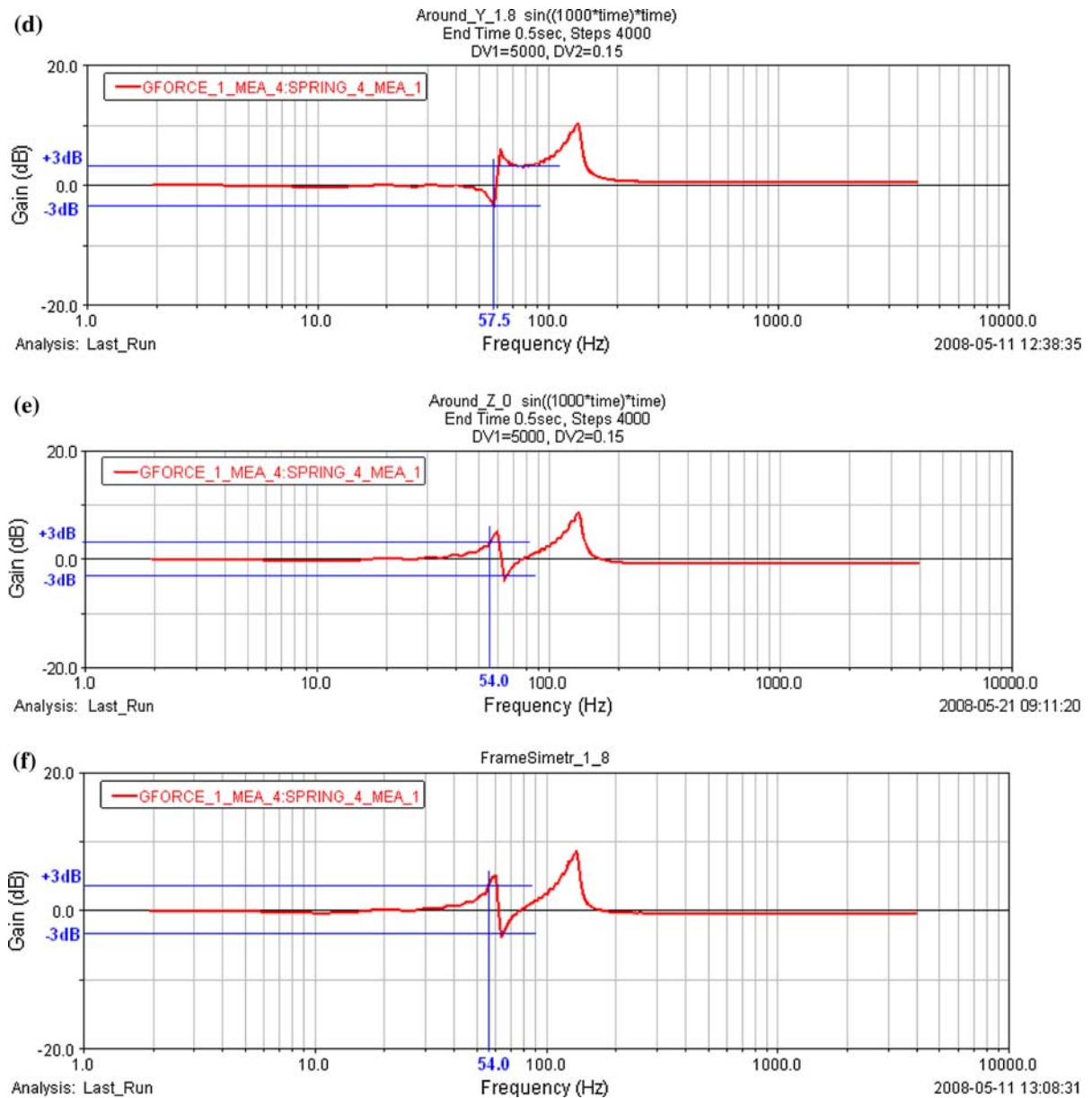


Fig. 20 continued

References

- Bentur, A., Berke, N.S., Diamond, S.: Diamond, Steel Corrosion in Concrete: Fundamentals and Civil Engineering Practice, 201 pp. Arnon Israel Sidney Diamond School of Civil Engineering, Purdue University, West Lafayette (1997)
- Chapsky, V., Portman, V., Sandler, B.-Z.: Single-mass 6-DOF isotropic accelerometer with segmented PSD sensors. *Sens. Actuators A* **135/2**, 558–569 (2007)
- Corliss, J.M., Cole, S.R.: Heavy gas conversion of the NASA Langley Transonic dynamics tunnel, NASA, Langley Research Center, Hampton, VA, AIAA-1998-2710, Advanced Measurement and Ground Testing Technology Conference, 20th, Albuquerque, NM, 15–18 June 1998
- Ewald, F.R.: Multi-component force balances for conventional and cryogenic wind tunnels. *Meas. Sci. Technol.* **11**, R81–R94 (2000)
- Gorlin, S.M., Slezinger, I.I.: Wind tunnels and their instrumentation, translated from Russian for NASA tt f-346.

- http://www.centennialofflight.gov/essay/Evolution_of_Technology/advanced_wind_tunnels/Tech36.htm (2000)
- Kerr, D.R.: Analysis, properties, and design of a Stewart-platform transducer” in transaction of the ASME. *J. Mech. Transm. Autom. Des.* **111/25**, 25–28 (1989)
- Liu, S.A., Tso, H.L.: A novel six-component force sensor of good measurement isotropy and sensitivities. *Sens. Actuators A* **100**, 223–230 (2002)
- Nguyen, C.C., Antrazi, S., Zhou, Z.-L., Campbell Jr., C.E.: Analysis and experimentation of a Stewart platform-based force/torque sensor. *Int. J. Robot. Autom.* **7**(3), 133–141 (1992)
- Pope, A., Harper, J.J.: *Low-Speed Wind Tunnel Testing*. Wiley, New York (1999)
- Sanderson, S.R., Simmons, J.M.: Force measurement in impulse facilities, Department of Mechanical Engineering, University of Queensland. http://www.mech.uq.edu.au/~mee/force_balances.html (2006)
- Tuttle, S.L., Mee, D.J., Simmons, J.M., Daniel W.J., et al.: “NASA technical reports”. <http://ntrs.nasa.gov/search.jsp> (1994)